

# Offset-electrode profile acquisition strategy for electrical resistivity tomography

Austin R. Robbins, Alain Plattner\*

Department of Earth and Environmental Sciences, California State University, Fresno, Fresno, CA 93740, USA

## ARTICLE INFO

### Article history:

Received 12 September 2017  
Received in revised form 23 January 2018  
Accepted 30 January 2018  
Available online 6 February 2018

### Keywords:

Electrical resistivity tomography  
2-D profiles  
3-D inversion  
Sensitivity pattern  
Field method

## ABSTRACT

We present an electrode layout strategy that allows electrical resistivity profiles to image the third dimension close to the profile plane. This “offset-electrode profile” approach involves laterally displacing electrodes away from the profile line in an alternating fashion and then inverting the resulting data using three-dimensional electrical resistivity tomography software. In our synthetic and field surveys, the offset-electrode method succeeds in revealing three-dimensional structures in the vicinity of the profile plane, which we could not achieve using three-dimensional inversions of linear profiles. We confirm and explain the limits of linear electrode profiles through a discussion of the three-dimensional sensitivity patterns: For a homogeneous starting model together with a linear electrode layout, all sensitivities remain symmetric with respect to the profile plane through each inversion step. This limitation can be overcome with offset-electrode layouts by breaking the symmetry pattern among the sensitivities. Thanks to freely available powerful three-dimensional resistivity tomography software and cheap modern computing power, the requirement for full three-dimensional calculations does not create a significant burden and renders the offset-electrode approach a cost-effective method. By offsetting the electrodes in an alternating pattern, as opposed to laying the profile out in a U-shape, we minimize shortening the profile length.

© 2018 Elsevier B.V. All rights reserved.

## 1. Introduction

Over the past few decades, electrical resistivity tomography (ERT) has been among the most popular geophysical methods for imaging the shallow subsurface. Its versatility has made it a viable technique for applications as diverse as aquifer characterization (e.g. Slater et al., 2000; Kemna et al., 2002; Coscia et al., 2011, 2012; Doetsch et al., 2010, 2012; Yeh et al., 2015), contamination monitoring (e.g. Ogilvy et al., 2003; Olofsson et al., 2006; Genelle et al., 2012; Bichet et al., 2016; Maurya et al., 2017), bedrock mapping (e.g. Cardarelli and De Donno, 2017; Chambers et al., 2012, 2013), soil science (see Samouëlian et al., 2005, for an overview), subsurface cavity detection (Leucci, 2006; Lazzari et al., 2010; Martínez-Pagán et al., 2013; Park et al., 2014; Bharti et al., 2016), landslide (e.g. Ling et al., 2016; Wilkinson et al., 2016) and rock avalanche investigations (e.g. Socco et al., 2010), studies of saline intrusion (Martínez et al., 2009; Goebel et al., 2017), volcanology (Revil, 2008; Barde-Cabusson et al., 2013; Brothelande et al., 2014), and archaeology (Astin et al., 2007; Ullrich et al., 2007; Negri et al., 2008; Himi et al., 2016; Nero et al., 2016).

Loke et al. (2013) provide an overview covering recent electrical resistivity tomography developments.

Freely available high-performance software packages for electrical resistivity tomography such as BERT (Günther et al., 2006; Rücker et al., 2006) and E4D (Johnson et al., 2010), cheap computing power, and improvements in algorithm design (e.g. Blome et al., 2009; Papadopoulos et al., 2011; Plattner et al., 2010, 2012) have made three-dimensional electrical resistivity data inversions cheaper than ever. Nevertheless, two-dimensional investigations imaging resistivity at depth along profile lines remain the most widely used electrical resistivity applications (Loke et al., 2013). The popularity of two-dimensional over three-dimensional surveys is likely a consequence of reduced equipment requirements and lower cost of work in the field. Developments in data acquisition strategies (e.g. Blome et al., 2011; Hoorde et al., 2017) and of the equipment itself (e.g. Stummer et al., 2002; Blome et al., 2011) help offset some of the extra cost of three-dimensional surveys in the field, but are unlikely to bridge the vast gap between the simplicity of two-dimensional profiles and the time required to set up and run a full 3-D array. To obtain subsurface resistivity models along profile lines, investigators typically make use of a “2.5-D” inversion procedure (Dey and Morrison, 1979), which implements a three-dimensional current source but assumes that subsurface resistivities only vary within the profile plane and

\* Corresponding author.

E-mail address: [plattner@alumni.ethz.ch](mailto:plattner@alumni.ethz.ch) (A. Plattner).

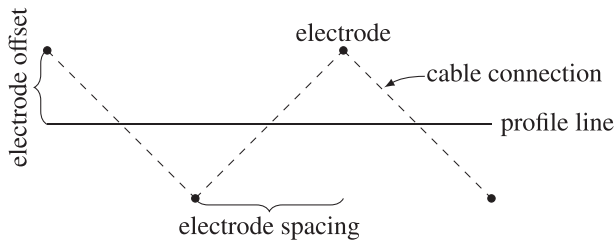


**Fig. 1.** Map-view schematic of the offset-electrode layout. Instead of placing the electrodes along the profile line, we move each electrode away from the profile line in an alternating pattern.

extend infinitely perpendicular to the plane. These 2.5-D inversions allow for a quick imaging of the subsurface along profile lines but are prone to artifacts and are unable to image resistivity variations beyond the profile plane.

We propose a cost-effective profile approach that has the capability of imaging the third dimension close to the profile plane. As we show in Section 3, simply inverting linear profile data using three-dimensional software does not suffice. Our approach involves staggering the electrodes on the surface surrounding the desired profile line, thus creating an asymmetry by which 3-D inversions may image variations in resistivity outside the profile plane. In Section 2 we further describe the field implementation of this electrode layout. We show the results from synthetic and field experiments in Sections 3 and 4, respectively. The results from the field surveys were presented in an extended abstract (Robbins and Plattner, 2017), here we provide additional context and explanations including a suite of computational experiments.

## 2. The offset-electrode profile method

Fig. 1 shows a map-view diagram of the electrode placement with respect to the profile line. Each electrode is moved away perpendicularly from the profile line. In the regular implementation of this layout, the electrode offset is staggered, such that odd-numbered and even-numbered electrodes are on opposite sides of the profile, forming a zigzag pattern. Alternatively, the offsets can be randomized. In its simplest form of constant offsets, the method can be implemented in the field by laying out parallel tape measures on either side of the profile as shown in the aerial photograph in Fig. 8(b).

## 3. Synthetic surveys

To test the effectiveness of laterally offsetting the electrodes, we ran computational experiments in which we simulated electrical resistivity field data for an artificially chosen subsurface resistivity distribution using the software E4D by Johnson et al. (2010). We then inverted the simulated “synthetic” survey data using the software BERT by Günther et al. (2006) and Rücker et al. (2006). As described by Colton and Kress (2013), when testing inversion methods using the same discretization and forward modeling procedure in the simulation of the data as in the inversion itself, we may bias the assessment. The inversion results from such a test may be better than what could be obtained using a different inversion discretization or forward modeling procedure. This “inversion crime” (Colton and Kress, 2013, p. 154) would hence lead to overly optimistic results for the performance of the inversion. Since electrical resistivity tomography is heavily underdetermined and therefore relies on regularization, we do not expect that using the same mesh and modeling method will strongly distort the results. Nevertheless

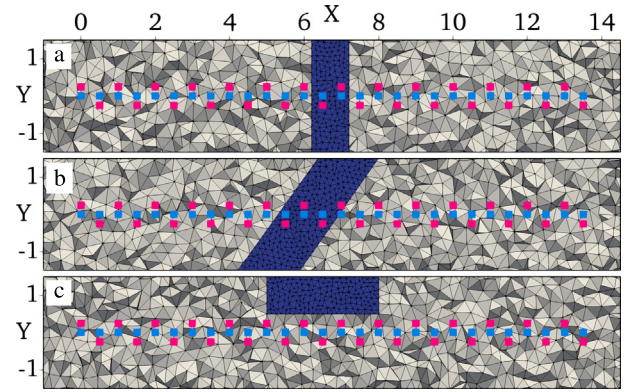


**Fig. 2.** Map views of slices at 0.5 m depth through the synthetic resistivity models used to test the effectiveness of offset-electrode profiles. Background electrical resistivity is 100  $\Omega\text{m}$  (gray), resistivity of the buried objects is 10  $\Omega\text{m}$  (blue). Light-blue dots indicate electrode positions for a conventional linear profile layout, magenta dots show electrode positions for the offset-electrode layout. Objects are buried at 10 cm depth and extend to 1 m depth. (a) Perpendicular profile intersection. (b) Oblique profile intersection. (c) Single-sided contrast. Axis units are in meters.

we decided to use different software packages and different meshes for data simulation and inversion to avoid such bias in our tests.

Fig. 2 shows the three subsurface resistivity distributions for the synthetic surveys. In Fig. 2(a), the conductive object (blue) intersects the profile line perpendicularly and therefore satisfies the 2.5-D inversion assumptions. The conductive object in Fig. 2(b) intersects the profile line obliquely, creating an asymmetry with respect to the profile plane. In Fig. 2(c), the conductive contrast lies entirely on one side of the profile, mimicking a situation often encountered when the precise location of the target is not known. We simulated data for both the Wenner and the dipole-dipole electrode array with a maximum dipole separation of six times dipole length (Dahlin and Zhou, 2004). We did not add noise to the synthetic data but set its estimated error, which was required for the inversion, to 2%. In the supplementary material for this article we provide all configuration and parameter files required by E4D and BERT to recreate the synthetic data and run all inversions shown in this section.

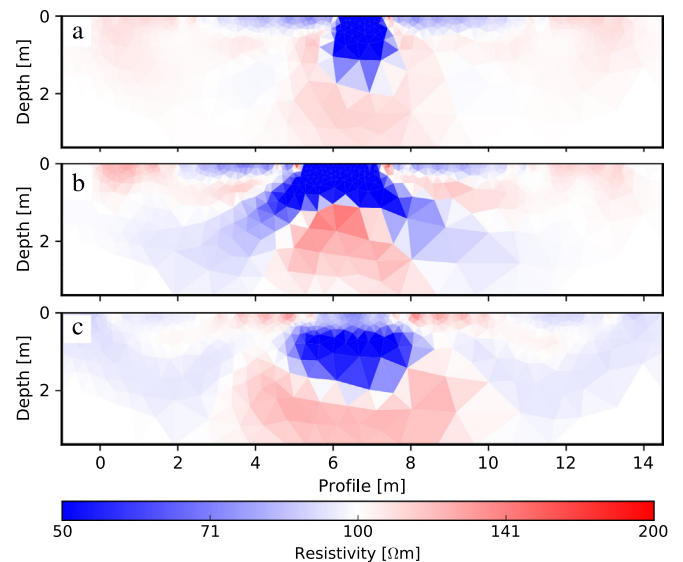


**Fig. 3.** 2.5-D inversion results for synthetic data obtained from the models shown in Fig. 2. (a) Result from perpendicularly intersecting object (Fig. 2a). (b) Result from obliquely intersecting object (Fig. 2b). (c) Result from single-sided object (Fig. 2c).

### 3.1. Linear layout, synthetic data, 2.5-D inversions

Fig. 3 shows the 2.5-D inversion results of the synthetic data calculated from the models in Fig. 2 for a linear electrode layout. All three inversions used the default regularization settings in BERT (see supplemental material for data, configuration, and log files). For the perpendicularly striking object in Fig. 2(a), the resulting 2.5-D profile shown in Fig. 3(a) correctly resolved the shape and location of the conductive contrast. On the other hand, for the object crossing the profile line obliquely in Fig. 2(b), the 2.5-D inversion result (Fig. 3b) shows artificial “pant legs” extending from both sides of the conductive contrast. Without knowledge of the oblique object, these pant legs could be misinterpreted as structure. Practitioners aim to avoid such artifacts by running profile lines perpendicularly to the most extended dimension of their target (Seidel and Lange, 2007) but the true structure of the subsurface is rarely known in advance of the survey. Fig. 3(c) shows the 2.5-D inversion result for the linear profile of the single-sided block example in Fig. 2(c). The block in the true model (Fig. 2c) is buried at 0.1 m depth and extends to 1 m. The inversion result incorrectly shows the top of the block at 0.5 m. In addition to misestimating the depth to target, the inversion result also contains artifacts below and on either side of the block. These examples show how strongly distorted 2.5-D inversion results can be when the subsurface resistivity contrasts do not extend perpendicularly from the profile.

### 3.2. Linear layout, synthetic data, 3-D inversions

To avoid assuming that the subsurface resistivity is constant perpendicularly to the profile plane, as is the case for 2.5-D inversions, we ran three-dimensional inversions of the same synthetic data as in Section 3.1. As for the 2.5-D inversions we used BERT’s default regularization. The inlay of Fig. 4(a) shows a horizontal slice at 0.5 m depth of the inversion result for the synthetic data obtained from the model given in Fig. 2(b) with a linear electrode layout. The black line indicates the contour for 30  $\Omega\text{m}$ . The meshed background of Fig. 4(a) shows the synthetic model for comparison. Despite using a three-dimensional inversion, the resistivity solution appears symmetric with respect to the profile plane. The same problem persists for the linear layout when the object is limited to one side of the profile (Fig. 2c). The inversion result shown in Fig. 4(b) (inlay) does not recognize the asymmetry of the original model (meshed background). No contour lines are visible in this panel because the resistivity values of the result are above 30  $\Omega\text{m}$ . In both examples, the three-dimensional inversions of linear profile data incorrectly yielded objects that were symmetric with respect to the profile plane, as opposed to an oblique intersection, or no intersection at all. To explain this discrepancy we must examine how typical electrical resistivity inversions generate resistivity models.

### 3.3. Inversion and sensitivities

To obtain a resistivity model from electrical resistivity data, we must select a starting model (typically a constant subsurface of average apparent resistivity) and provide additional constraints in the form of regularization (e.g. model-update damping and structural smoothing). Fig. 6 shows a flowchart for a typical electrical resistivity tomography algorithm. In a first step, the algorithm sets the starting model as the assumed subsurface electrical resistivity distribution (“model”). It then calculates (depending on model, data, electrode information, and regularization) a model update to better fit the measured data. In further iterations, the updated model is used as the assumed subsurface electrical resistivity distribution and the process is repeated until either the simulated data fit the measured data up to noise level, or the model update leads to little

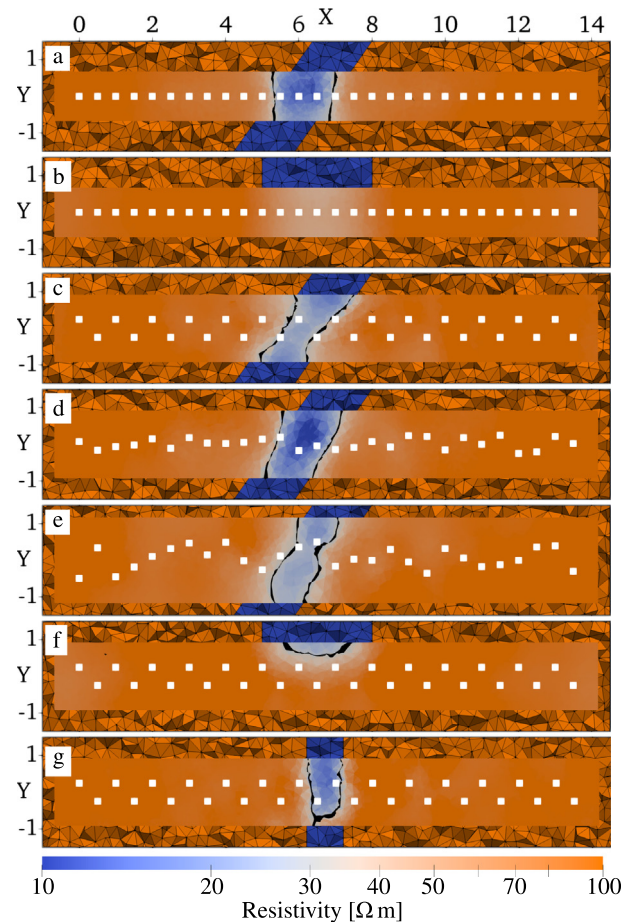


**Fig. 4.** Map views of synthetic models (meshed backgrounds) and inversion results (inlays) sliced at 0.5 m depth. Black lines denote contours at 30  $\Omega\text{m}$ . Electrodes are indicated by white squares. (a) Linear electrode layout for oblique object (Fig. 2b). (b) Linear electrode layout for single-sided block (Fig. 2c). (c)–(e) Regular and random offset-electrode layouts for oblique object (Fig. 2b). (f) Regular offset electrode layout for single-sided block (Fig. 2c). (g) Regular offset-electrode layout for perpendicular object (Fig. 2a).

change. See for example Günther et al. (2006) for a detailed mathematical description of this procedure. As indicated in Fig. 6, the model update in each inversion step depends on the “sensitivities” or “Jacobian matrix”. For each measured datum, the corresponding sensitivity pattern describes how a variation in the subsurface resistivity influences the value of this datum. The sensitivities depend on the model, electrode positions, and electrode configuration.

To illustrate the effect of sensitivities on the model update we show, in Fig. 7, sensitivity patterns for select electrode combinations calculated for a homogeneous resistivity (a typical starting model). Fig. 7(a) shows the sensitivity pattern, cut at 0.5 m depth,

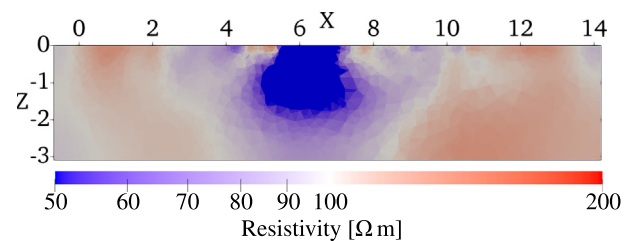


**Fig. 5.** Vertical slice through the inversion result shown in Fig. 4(c) along the  $Y = 0$  axis with color scheme as in Fig. 3. X-axis is along profile, Z-axis is depth. Axis units are in meters.



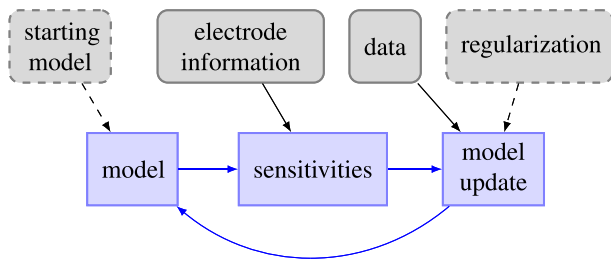


**Fig. 6.** Inversion flowchart. Gray indicates user input either recorded in the field (solid boundary) or chosen for the inversion (dashed boundary). Blue indicates algorithm-controlled entities. Electrode information includes electrode position and configuration. The algorithm iterates through the blue cycle until either synthetic data fit the measured data within estimated errors, or the model update is insignificantly small.

for a dipole-dipole measurement using the current injection electrodes at 0.5 m and 1 m and potential electrodes at 1.5 m and 2 m for a linear electrode layout. Fig. 7(b) shows the sensitivity pattern for the same setup as in Fig. 7(a) but for current injection electrodes at 1 m and 2.5 m and potential electrodes at 10 m and 11.5 m. Both of these sensitivity patterns are symmetric with respect to the profile plane indicated by the white line. This symmetry is a result of the dependence of sensitivities on electrical potential fields from a given subsurface resistivity distribution and current electrode position. Potential fields for symmetric resistivity patterns with the current electrode positioned on the symmetry plane carry the same symmetry as the resistivity pattern (see e.g. the derivations by Rücker et al., 2006). The sensitivity pattern of a single source-receiver pair is defined as the derivative of the measured potential field with respect to each model parameter cell. This pattern can be calculated via the inner product of the spatial gradients of the potential fields for the electrodes (see e.g. Günther et al., 2006), and is therefore also symmetric for symmetric potential fields with both electrodes on the axis of symmetry. Finally, the sensitivity pattern of an electrode combination is simply a linear combination of the sensitivity patterns for the individual electrode pairs. If all sensitivity patterns carry the same symmetry, then their linear combinations will also carry that symmetry. This causes the model update for linear electrode layouts from a model that is symmetric with respect to the profile plane and with all electrodes on the profile plane to be symmetric. In return, this leads again to symmetric sensitivities from the updated model (see Fig. 6). The sensitivity patterns in Fig. 7 are all calculated for a homogeneous resistivity model but any sensitivity pattern for resistivity models that are symmetric with respect to the profile plane and with all electrodes on the profile axis will carry the same symmetry.

#### 3.4. Offset electrodes, synthetic data, 3-D inversions

We break the cycle of symmetry by alternately offsetting the electrodes away from the profile. Each sensitivity pattern for a single measurement may still carry a symmetry but the symmetries vary among the measurements. Fig. 7(c) and (d) show the offset-electrode sensitivity patterns for the same electrode combinations as Fig. 7(a) and (b), again for a homogeneous resistivity model. Each of the sensitivity patterns shown in Fig. 7(c) and (d) for the offset-electrode layout contains a symmetry, but not the same kind. As a consequence, the combination of the sensitivities for offset electrodes allows the algorithm to distinguish on which side of the profile an electrical resistivity contrast is located. The maximally resolvable distance from the profile depends on the electrode offset and the subsurface resistivity distribution. Fig. 4(c–e) show inversion results for the offset-electrode approach for synthetic data created as described in the beginning of Section 3 for the model shown in Fig. 2(b). For Fig. 4(c) we selected a regular “zigzag” offset approach

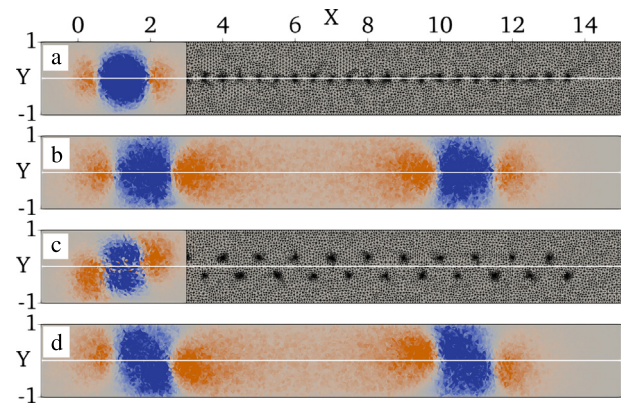


**Fig. 7.** Sensitivity patterns at 0.5 m depth for various dipole-dipole measurements comparing the linear layout to the offset-electrode layout. Electrode positions are indicated by locations with fine mesh. The white line indicates the axis of the linear electrode layout. Blue is negative sensitivity, red positive. Color range is symmetric and adapted for each panel. (a) Sensitivity pattern for linear layout with injection electrodes 2 and 3, potential electrodes 4 and 5. (b) Sensitivity pattern for linear layout with injection electrodes 6 and 3, potential electrodes 21 and 24. (c) Offset-electrode layout for same setting as in panel (a). (d) Offset-electrode layout for same setting as in panel (b).

with electrode offset 0.25 m. For Fig. 4(d) and (e), we picked randomly distributed offsets that follow a uniform distribution with maximum offset distance 0.25 m for Fig. 4(d) and maximum offset distance 0.5 m for Fig. 4(e). Each of the three offset examples for the obliquely intersecting object performs better than the linear layout shown in Fig. 4(a). The regular offset in Fig. 4(c) best detected the orientation of the object but underestimated the resistivity contrast of the object. The short-offset random layout in Fig. 4(d) best recovered the resistivity value but not the orientation of the object. The long-offset random layout in Fig. 4(e) recovered that there is a conductive object intersecting at an oblique angle but does not correctly recover its shape or resistivity. For the single-sided box model shown in Fig. 2(c), the regular offset electrode result in Fig. 4(f) correctly identified that the conductive object is only present on one side of the profile. This was not possible with the linear electrode layout (Fig. 4b). To demonstrate that the offset-electrode layout does not have a disadvantage over the linear layout in the special case when the subsurface is truly symmetric with respect to the profile line, we inverted synthetic data for a regular offset-electrode profile and a perpendicularly striking object. As we show in Fig. 4(g), the inversion correctly reconstructed the orientation of the object.

The 2.5-D inversion result of the obliquely intersecting object in Fig. 3 contained artifacts known as “pant legs”. In Fig. 5 we show a vertical section through the inversion result of Fig. 4(c). The offset-electrode inversion result does not contain the pant legs visible in the 2.5-D inversion.

#### 4. Field surveys

To test the real-world performance of offset electrodes we collected both linear profile and regularly offset (zigzag) profile data on California State University Fresno campus. Utility construction several Months prior led to a backfilled trench with a visibly replaced sod. Aerial imagery of the site in Fig. 8(a) and (b), taken with a drone, shows the replaced sod traversing the image obliquely and intersecting the profile line roughly at its center. The trench itself was narrower than the replaced sod and is located at its center. The images also show the sideline markings of a football practice field, as well as the corner of a utility box and a concrete curb in the upper right corner. Magenta dots represent the electrodes for a linear (Fig. 8a) and offset-electrode (Fig. 8b) profile layout. Electrode

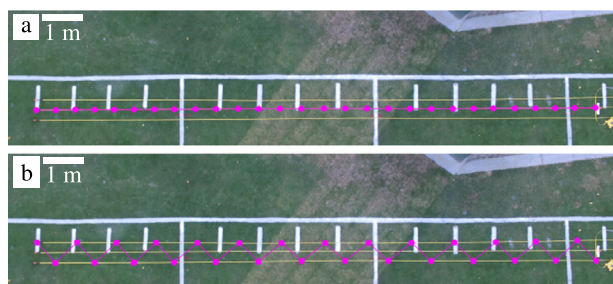


**Fig. 8.** Aerial photograph of the field survey site and electrode positioning (purple dots) for a linear profile (a), and a regularly offset (zigzag) profile (b). White lines are marks of a practice football field. Discolored grass is recently replaced sod after trenching for utilities construction. Tape measures on either side of the profile line helped accurately offset the electrodes.

spacing is 0.5 m with offsets of 0.25 m in Fig. 8(b). From observations during the excavation, we conclude that the subsurface spatial relationships between the soil backfill and the profile resemble the ideal case of our synthetic surveys in Section 3. However, the Months since completion of the construction together with rain have likely led to a weakening and possibly distortion of the resistivity contrast.

For each of the two profiles shown in Fig. 8 we collected Wenner and dipole-dipole data using an AGI SuperSting R1 system with 28 electrodes and inverted the data as described in Section 3 using the software E4D. We inverted for the electrical resistivity distribution within a rectangle with x-axis (along-profile) limits  $-1$  to  $15$  m and y-axis limits  $-1$  to  $1$  m. To avoid numerical boundary effects, we padded our modeling region with a coarsely discretized external domain extending up to  $50$  m away from the origin. Overall, our inversion mesh contained 988 313 tetrahedral cells. We regularized the inversions of the field data using the “Smoothness Constrained Inversion” options file provided in the E4D User Guide. Both, the linear and the offset-electrode inversion converged to a targeted  $\chi^2$  value of 1 within 8 and 12 iterations respectively, indicating that we fitted the data to their estimated errors. Fig. 9 shows horizontal slices of the resulting resistivity models at  $0.5$  m depth plotted over the aerial photographs from Fig. 8. See supplemental material for raw data, E4D configuration files, and inversion logs.

In the electrical resistivity inversion result for the linear electrode layout shown in Fig. 9(a) we observe a prominent conductive resistivity contrast coinciding with the intersection of the replaced sod and our profile line. Reminiscent of the results in Fig. 4(a), we interpret this conductive contrast as the backfilled trench underneath the replaced sod. As in the synthetic case in Fig. 4(a), the resulting

conductive feature is symmetric with respect to the profile plane. Fig. 9(b) shows the field result for the offset-electrode profile layout from Fig. 8(b). Here the conductive feature does not intersect the profile perpendicularly but at an oblique angle. The  $30 \Omega\text{m}$  contour lines on either side of the contrast within the replaced sod appear roughly parallel to the sod on the upper part of the model (side of the concrete curb). In the lower part, the contour line to the right hand side deviates. We further observe a resistive feature toward the right edge of the profile. In Fig. 9(a), the resistive feature is symmetric with respect to the profile plane but in Fig. 9(b), it appears to be shifted toward the concrete curb.

## 5. Discussion and conclusions

From our synthetic and field surveys, we conclude that offset-electrode profiles can image three-dimensional structures close to the profile plane, which is not possible with linear profiles. Our method uses the same number of electrodes as its linear counterpart and therefore has a much lower field cost compared to full three-dimensional or multi-profile surveys. Compared to linear profiles, the maximum length of an offset-electrode profile, limited by take-out connector spacing, is shortened by a factor of  $\sqrt{1 + (2y/x)^2}$ , where  $x$  denotes the electrode spacing and  $y$  is the electrode offset (see Fig. 1). This shortening is less than the shortening using a U-shaped electrode layout (as used, for example, in the first step of a three-dimensional roll-along strategy). The U-shaped layout shortens the maximal profile length by a factor of 2.

Offset-electrode profiles lend themselves to “shifting offset” strategies, where after collection of data for one offset, the offset can be increased or decreased and a second data set with a different offset can be collected. Maximally resolvable depths depend on the maximum distance between electrodes, the subsurface resistivity distribution, and on the choice of the electrode array (e.g. Stummer et al., 2004). We therefore expect the maximally achievable depths of offset-electrode profiles to be similar to those of linear profiles. Here we used the Wenner and the dipole-dipole electrode arrays which were designed for linear profiles. Electrode array optimization investigations such as for example the work of Stummer et al. (2004) and Blome et al. (2011) for three-dimensional layouts may lead to tailored configurations for offset-electrode profiles.

Our field survey using the offset-electrode array shown in Fig. 9(b) recovered a contrast that roughly aligned with the expected direction but the alignment was not perfect. This may be a consequence of changes in the soil since implacement during utility construction several months ago, or from data noise.

Determining an optimal electrode offset distance will depend on the specifics of a survey and on which parameters are most important to the investigator. In our synthetic surveys, short offsets led to a better reconstruction of the target’s resistivity value but its shape was incorrectly imaged (Fig. 4d). Too large offsets did not help reconstruct the target’s shape (Fig. 4e). An electrode offset of half the electrode spacing led to a good reconstruction of the target shape but underestimated the resistivity contrast (Fig. 4c). Offsetting the electrodes by randomly varying distances as shown in Fig. 4(d) and (e) may help avoid artifacts caused by the regularity of the electrode placement. In practice it may be easier in the field to implement a regular (zigzag) offset-electrode approach as shown in Fig. 4(c) since this avoids the need to record the exact position of each electrode. We note that all offset-electrode profiles in Fig. 4(c)–(f) correctly identified the asymmetry of the subsurface, unlike the linear profiles (Fig. 4a,b). The essence of this approach is that offsetting the electrodes breaks the common symmetry of the measurement sensitivity patterns. We therefore expect offset-electrodes to also map off-profile resistivity variations for large electrode spacing, if the electrode offset is increased accordingly. For applications with a specific expected subsurface resistivity model, we recommend running

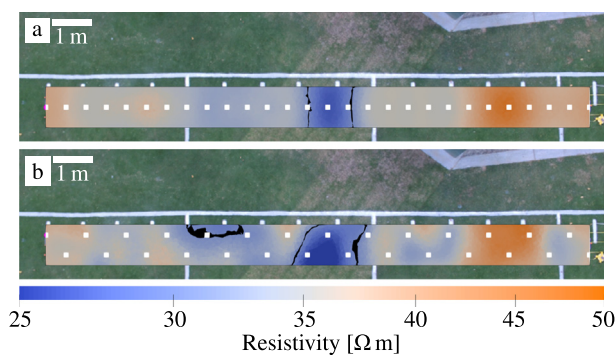


**Fig. 9.** Map-views of three-dimensional inversion results, cut at  $0.5$  m depth. Black lines denote contours at  $30 \Omega\text{m}$ . White squares show the electrode positions for (a) linear electrode layout and (b) offset-electrode layout.

synthetic surveys such as the ones presented here to determine a suitable electrode offset. E4D (Johnson et al., 2010) allows for simulation of data for almost arbitrarily complex resistivity models. The scripts by Plattner (2017b) facilitate setting up the mesh constraints for E4D simulations.

When comparing the susceptibility to noise of our offset electrode approach to the classical profile, we note that by removing the symmetry, we indeed increase the variance of the solution. We additionally allow asymmetric variations of the subsurface resistivity and therefore effectively increase the degrees of freedom. At the same time we reduce bias by removing the enforcement of symmetry with respect to the profile line.

Offset-electrode profile data requires three-dimensional electrical resistivity tomography software for inversion. Several powerful implementations are freely available (e.g. BERT and E4D: Rücker et al., 2006; Günther et al., 2006; Johnson et al., 2010). See Plattner (2017a,b) for additional BERT and E4D tools and tutorials. The two-dimensional discretization required for 2.5-D inversions leads to a smaller number of subsurface resistivity cells and hence lower computational cost compared to a full three-dimensional inversion. In our offset-electrode profile inversions, we built three-dimensional meshes only within a narrow band along the profile, hence limiting the number of cells compared to a full three-dimensional inversion. With computing power becoming increasingly cheap, the computational advantage of two-dimensional over three-dimensional meshes is diminishing.

## Acknowledgments

The authors thank Tim Johnson for his software E4D, and for adding the option to write out sensitivities, Thomas Günther and Carsten Rücker for their program BERT, and the Geoscience Department at Princeton University for hosting. We also thank Christine Liu and Alexandre Briand for their assistance in the field. A. R. R. thanks the Fresno State Associated Students, Inc. and the Fresno State College of Science and Mathematics for the research funding through student grants. This material is based upon work supported by the National Science Foundation under grant no. EAR-1550732.

## References

- Astin, T., Eckardt, H., Hay, S., 2007. Resistivity imaging survey of the Roman barrows at Bartlow, Cambridgeshire, UK. *Archaeol. Prospect.* 14, 24–37. <https://doi.org/10.1002/arp.287>.
- Barde-Cabusson, S., Bolós, X., Pedrazzi, D., Lovera, R., Serra, G., Martí, J., Casas, A., 2013. Electrical resistivity tomography revealing the internal structure of monogenetic volcanoes. *Geophys. Res. Lett.* 40, 2544–2549. <https://doi.org/10.1002/grl.50538>.
- Bharti, A.K., Pal, S.K., Priyam, P., Kumar, S., Srivastava, S., Yadav, P.K., 2016. Subsurface cavity detection over Patherdih colliery, Jharia Coalfield, India using electrical resistivity tomography. *Environ. Earth. Sci.* 75, 1–17. <https://doi.org/10.1007/s12665-015-5025-z>.
- Bichet, V., Grisey, E., Aleya, L., 2016. Spatial characterization of leachate plume using electrical resistivity tomography in a landfill composed of old and new cells (Belfort, France). *Eng. Geol.* 211, 61–73. <https://doi.org/10.1016/j.enggeo.2016.06.026>.
- Blome, M., Maurer, H., Greenhalgh, S., 2011. Geoelectric experimental design - efficient acquisition and exploitation of complete pole-bipole data sets. *Geophysics* 76, F15–F26. <https://doi.org/10.1190/1.3511350>.
- Blome, M., Maurer, H., Schmidt, K., 2009. Advances in three-dimensional geoelectric forward solver techniques. *Geophys. J. Int.* 176, 740. <https://doi.org/10.1111/j.1365-246X.2008.04006.x>.
- Brothelande, E., Finizola, A., Peltier, A., Delcher, E., Komorowski, J.C., Di Gangi, F., Borgogno, G., Passarella, M., Trovato, C., Legendre, Y., 2014. Fluid circulation pattern inside La Soufrière volcano (Guadeloupe) inferred from combined electrical resistivity tomography, self-potential, soil temperature and diffuse degassing measurements. *J. Volcanol. Geoth. Res.* 288, 105–122. <https://doi.org/10.1016/j.jvolgeores.2014.10.007>.
- Cardarelli, E., De Donno, G., 2017. Multidimensional electrical resistivity survey for bedrock detection at the Rieti Plain (Central Italy). *J. Appl. Geoph.* 141, 77–87. <https://doi.org/10.1016/j.jappgeo.2017.04.012>.
- Chambers, J.E., Wilkinson, P.B., Wardrop, D., Hameed, A., Hill, I., Jeffrey, C., Loke, M., Meldrum, P., Kuras, O., Cave, M., Gunn, D.A., 2012. Bedrock detection beneath river terrace deposits using three-dimensional electrical resistivity tomography. *Geomorphology* 177–178, 17–25. <https://doi.org/10.1016/j.geomorph.2012.03.034>.
- Chambers, J.E., Wilkinson, P.B., Penn, S., Meldrum, P.I., Kuras, O., Loke, M.H., Gunn, D.A., 2013. River terrace sand and gravel deposit reserve estimation using three-dimensional electrical resistivity tomography for bedrock surface detection. *J. Appl. Geoph.* 93, 25–32. <https://doi.org/10.1016/j.jappgeo.2013.03.002>.
- Colton, D., Kress, R., 2013. *Inverse Acoustic and Electromagnetic Scattering Theory*. 3rd edition, Applied Mathematical Sciences vol. 93. Springer.
- Coscia, I., Greenhalgh, S.A., Linde, N., Doetsch, J., Marescot, L., Günther, T., Vogt, T., Green, A.G., 2011. 3D crosshole ERT for aquifer characterization and monitoring of infiltrating river water. *Geophysics* 76, G49–G59. <https://doi.org/10.1190/1.3553003>.
- Coscia, I., Linde, N., Greenhalgh, S., Vogt, T., Green, A., 2012. Estimating traveltimes and groundwater flow patterns using 3d time-lapse crosshole ERT imaging of electrical resistivity fluctuations induced by infiltrating river water. *Geophysics* 77, E239–E250. <https://doi.org/10.1190/geo2011-0328.1>.
- Dahlin, T., Zhou, B., 2004. A numerical comparison of 2D resistivity imaging with 10 electrode arrays. *Geophys. Prospect.* 52, 379–398. <https://doi.org/10.1111/j.1365-2478.2004.00423.x>.
- Dey, A., Morrison, H., 1979. Resistivity modeling for arbitrarily shaped two-dimensional structures. *Geophys. Prospect.* 27, 106–136. <https://doi.org/10.1111/j.1365-2478.1979.tb00961.x>.
- Doetsch, J., Linde, N., Coscia, I., Greenhalgh, S.A., Green, A.G., 2010. Zonation for 3D aquifer characterization based on joint inversions of multimethod cross-hole geophysical data. *Geophysics* 75, G53–G64. <https://doi.org/10.1190/1.3496476>.
- Doetsch, J., Linde, N., Pessognelli, M., Green, A.G., Günther, T., 2012. Constraining 3-D electrical resistance tomography with GPR reflection data for improved aquifer characterization. *J. Appl. Geoph.* 78, 68–76. <https://doi.org/10.1016/j.jappgeo.2011.04.008>.
- Genelle, F., Sirieix, C., Riss, J., Naudet, V., 2012. Monitoring landfill cover by electrical resistivity tomography on an experimental site. *Eng. Geol.* 145–146, 18–29. <https://doi.org/10.1016/j.enggeo.2012.06.002>.
- Goebel, M., Pidlisecky, A., Knight, R., 2017. Resistivity imaging reveals complex pattern of saltwater intrusion along Monterey coast. *J. Hydrol.* 551, 746–755. <https://doi.org/10.1016/j.jhydrol.2017.02.037>.
- Günther, T., Rücker, C., Spitzer, K., 2006. Three-dimensional modelling and inversion of dc resistivity data incorporating topography - II. Inversion. *Geophys. J. Int.* 166, 506. <https://doi.org/10.1111/j.1365-246X.2006.03011.x>.
- Himi, M., Armendariz, A., Teira, L., Gonzalez, J., Ibanez, J., Haidar-Boustani, M., Casas, A., 2016. Geophysical and archaeological evidences of buried epipalaeolithic, neolithic, bronze age and Roman architecture in West-Central Syria. *Archaeol. Prospect.* 23, 273–285. <https://doi.org/10.1002/arp.1543>.
- Hoorde, M.V., Hermans, T., Dumont, G., Nguyen, F., 2017. 3D electrical resistivity tomography of karstified formations using cross-line measurements. *Eng. Geol.* 220, 123–132. <https://doi.org/10.1016/j.enggeo.2017.01.028>.
- Johnson, T.C., Versteeg, R.J., Ward, A., F.D., Day-Lewis, Revil, A., 2010. Improved hydro-geophysical characterization and monitoring through parallel modeling and inversion of time-domain resistivity and induced polarization data. *Geophysics* 74, Wa27–Wa41. <https://doi.org/10.1190/1.3475513>.
- Kemna, A., Vanderborght, J., Kulesa, B., Vereecken, H., 2002. Imaging and characterisation of subsurface solute transport using electrical resistivity tomography (ERT) and equivalent transport models. *J. Hydrol.* 267, 125–146. [https://doi.org/10.1016/S0022-1694\(02\)00145-2](https://doi.org/10.1016/S0022-1694(02)00145-2).
- Lazzari, M., Loperte, A., Perrone, A., 2010. Near surface geophysics techniques and geomorphological approach to reconstruct the hazard cave map in historical and urban areas. *Adv. Geosci.* 24, 35–44. <https://doi.org/10.5194/advgeo-24-35-2010>.
- Leucci, G., 2006. Contribution of ground penetrating radar and electrical resistivity tomography to identify the cavity and fractures under the main Church in Botrugno (Lecce, Italy). *J. Archaeol. Sci.* 33, 1194–1204. <https://doi.org/10.1016/j.jas.2005.12.009>.
- Ling, C., Xu, Q., Zhang, Q., Ran, J., Lv, H., 2016. Application of electrical resistivity tomography for investigating the internal structure of a translational landslide and characterizing its groundwater circulation (Kualiangzi landslide, Southwest China). *J. Appl. Geoph.* 131, 154–162. <https://doi.org/10.1016/j.jappgeo.2016.06.003>.
- Loke, M.H., Chambers, J.E., Rucker, D.F., Kuras, O., Wilkinson, P.B., 2013. Recent developments in the direct-current geoelectrical imaging method. *J. Appl. Geoph.* 95, 135–156. <https://doi.org/10.1016/j.jappgeo.2013.02.017>.
- Martínez, J., Benavente, J., García-Aróstegui, J.I., Hidalgo, M.C., Rey, J., 2009. Contribution of electrical resistivity tomography to the study of detrital aquifers affected by seawater intrusion-extrusion effects: the river Vélez delta (Vélez-Málaga, southern Spain). *Eng. Geol.* 108, 161–168. <https://doi.org/10.1016/j.enggeo.2009.07.004>.
- Martínez-Pagán, P., Gómez-Ortiz, D., Martín-Crespo, J., Manteca, J.I., Rosique, M., 2013. The electrical resistivity tomography method in the detection of shallow mining cavities. A case study on the Victoria Cave, Cartagena (SE Spain). *Eng. Geol.* 156, 1–10. <https://doi.org/10.1016/j.enggeo.2013.01.013>.
- Mauriya, P.K., Ronde, V.K., Fiandaca, G., Balbarini, N., Auken, E., Bjerg, P.L., Christiansen, A.V., 2017. Detailed landfill leachate plume mapping using 2D and 3D electrical resistivity tomography - with correlation to ionic strength measured in screens. *J. Appl. Geoph.* 138, 1–8. <https://doi.org/10.1016/j.jappgeo.2017.01.019>.



- Negri, S., Leucci, G., Mazzone, F., 2008. High resolution 3D ERT to help GPR data interpretation for researching archaeological items in a geologically complex subsurface. *J. Appl. Geoph.* 65, 111–120. <https://doi.org/10.1016/j.jappgeo.2008.06.004>.
- Nero, C., Aning, A.A., Danuor, S.K., Noye, R.M., 2016. Delineation of graves using electrical resistivity tomography. *J. Appl. Geoph.* 126, 138–147. <https://doi.org/10.1016/j.jappgeo.2016.01.012>.
- Ogilvy, R., Meldrum, P., Chambers, J., Williams, G., 2003. The use of 3D electrical resistivity tomography to characterise waste and leachate distribution within a closed landfill, Thriplow, UK. *J. Environ. Eng. Geoph.* 7, 11–18. <https://doi.org/10.4133/JEEG7.1.11>.
- Olofsson, B., Jernberg, H., Rosenqvist, A., 2006. Tracing leachates at waste sites using geophysical and geochemical modelling. *Environ. Geol.* 49, 720–732. <https://doi.org/10.1007/s00254-005-0117-9>.
- Papadopoulos, N., Tsourlos, P., Papazachos, C., Tsokas, G., Sarris, A., Kim, J., 2011. An algorithm for fast 3D inversion of surface electrical resistivity tomography data: application on imaging buried antiquities. *Geophys. Prospect.* 59, 557–575. <https://doi.org/10.1111/j.1365-2478.2010.00936.x>.
- Park, M.K., Park, S., Yi, M., Kim, C., Son, J., Kim, J., 2014. Application of electrical resistivity tomography (ERT) technique to detect underground cavities in a karst area of South Korea. *Environ. Earth. Sci* 71, 2797–2806. <https://doi.org/10.1007/s12665-013-2658-7>.
- Plattner, A., 2017a. BERTtools. <https://doi.org/10.5281/zenodo.821604>.
- Plattner, A., 2017b. E4Dtools. <https://doi.org/10.5281/zenodo.821598>.
- Plattner, A., Maurer, H., Vorloeper, J., Dahmen, W., 2010. Three-dimensional geoelectric modelling with optimal work/accuracy rate using an adaptive wavelet algorithm. *Geophys. J. Int.* 182, 741. <https://doi.org/10.1111/j.1365-246X.2010.04677.x>.
- Plattner, A., Maurer, H., Vorloeper, J., Blome, M., 2012. 3-D electrical resistivity tomography using adaptive wavelet parameter grids. *Geophys. J. Int.* 189, 317–330. <https://doi.org/10.1111/j.1365-246X.2012.05374.x>.
- Revil, A., 2008. Inner structure of La Fossa di Vulcano (Vulcano Island, southern Tyrrhenian Sea, Italy) revealed by high-resolution electric resistivity tomography coupled with self-potential, temperature, and CO<sub>2</sub> diffuse degassing measurements. *J. Geophys. Res.* 43, 1166–1174. <https://doi.org/10.1029/2007JB005394>.
- Robbins, A., Plattner, A., 2017. 2.75-D ERT: Zigzag electrode acquisition strategy to improve 2-D profiles. *Symposium on the Application of Geophysics to Engineering and Environmental Problems 2017*. Society of Exploration Geophysicists and Environment and Engineering Geophysical Society., pp. 183–187. <https://doi.org/10.4133/SAGEEP.30-007>.
- Rücker, C., Günther, T., Spitzer, K., 2006. Three-dimensional modelling and inversion of dc resistivity data incorporating topography - I. Modelling. *Geophys. J. Int.* 166, 495. <https://doi.org/10.1111/j.1365-246X.2006.03010.x>.
- Samouëlian, A., Cousin, I., Tabbagh, A., Bruand, A., Richard, G., 2005. Electrical resistivity survey in soil science: a review. *Soil Till. Res.* 83, 173–193. <https://doi.org/10.1016/j.still.2004.10.004>.
- Seidel, K., Lange, G., 2007. Direct current resistivity methods. In: Knödel, K., Lange, G., Voigt, H.J. (Eds.), *Environmental Geology: Handbook of Field Methods and case studies*. Springer., pp. 205–238.
- Slater, L., Binley, A., Daily, W., Johnson, R., 2000. Cross-hole electrical imaging of a controlled saline tracer injection. *J. Appl. Geoph.* 4, 85–102. [https://doi.org/10.1016/S0926-9851\(00\)00002-1](https://doi.org/10.1016/S0926-9851(00)00002-1).
- Socco, L.V., Jongmans, D., Boiero, D., Stocco, S., Maraschini, M., Tokeshi, K., Hantz, D., 2010. Geophysical investigation of the Sandalp rock avalanche deposits. *J. Appl. Geoph.* 70, 277–291. <https://doi.org/10.1016/j.jappgeo.2009.12.005>.
- Stummer, P., Maurer, H., Green, A.G., 2004. Experimental design: electrical resistivity data sets that provide optimum subsurface information. *Geophysics* 69, 120–139. <https://doi.org/10.1190/1.1649381>.
- Stummer, P., Maurer, H., Horstmeyer, H., Green, A.G., 2002. Optimization of DC resistivity data acquisition: real-time experimental design and a new multielectrode system. *IEEE Trans. Geosci. Remote Sens.* 40, 2727–2735. <https://doi.org/10.1109/TGRS.2002.807015>.
- Ullrich, B., Günther, T., Rücker, C., 2007. Electrical resistivity tomography methods for archaeological prospection. In: Posluschny, A., Lambers, K., Herzog, I. (Eds.), *Layers of Perception. Proceedings of the 35th International Conference on Computer Applications and Quantitative Methods in Archaeology (CAA)*. Berlin, Germany.
- Wilkinson, P., Chambers, J., Uhlemann, S., Meldrum, P., Smith, A., Dixon, N., Loke, M.H., 2016. Reconstruction of landslide movements by inversion of 4-D electrical resistivity tomography monitoring data. *Geophys. Res. Lett.* 43, 1166–1174. <https://doi.org/10.1002/2015GL067494>.
- Yeh, H., Lin, H., Wu, C., Hsu, K., Lee, J., Lee, C., 2015. Electrical resistivity tomography applied to groundwater aquifer at downstream of Chih-Ben Creek basin, Taiwan. *Environ. Earth. Sci* 73, 4681–4687. <https://doi.org/10.1007/s12665-014-3752-1>.